PNAS
www.pnas.org

Supplementary Information for

Hydrothermal synthesis of long-chain hydrocarbons up to C_{24} with $NaHCO_3$-assisted stabilizing cobalt

Daoping He, Xiaoguang Wang, Yang Yang, Runtian He, Heng Zhong, Ye Wang, Buxing Han, Fangming Jin

Fangming Jin; Heng Zhong; Buxing Han

Email: fmjin@sjtu.edu.cn; zhong.h@sjtu.edu.cn; hanbx@iccas.ac.cn

This PDF file includes:

Table S1. Comparison of natural alkaline hydrothermal environment and our hydrothermal system. The low concentration of dissolved inorganic carbon in actual hydrothermal environment is due to its reduction to hydrocarbons and the precipitation of inorganic mineral deposits such as calcium carbonate. The choice of high concentration bicarbonate in the simulated environment is based on the following considerations. First, the high concentration bicarbonate can act as a strong buffer to maintain the pH thus to maintain the dominant species. Second, the high concentration bicarbonate can enhance the oxidation of Fe to generate H_2 thus to create a high-pressure reaction environment.

Entry	pH	Carbon source	Concentration (M)	Temperature (°C)	Pressure (MPa)
Natural alkaline hydrothermal environment (1-7)	9~11	HCO_3^-	0.012~0.03	≤ 400, a typical value is ~300	≤ 100, a typical value is ~35
Our system	8.23~9.30	HCO_3^-	1.15	300	30

Table S2. Effect of different transition metal/metal oxide additives on the formation of organic compounds from HCO_3^-. The addition of Mo, TiO_2, ZnO and Al_2O_3 failed to generate new products except for $HCOO^-$. The addition of Ni promoted the formation of methane. Experimental conditions: Fe, 80 mmol; $NaHCO_3$, 80 mmol; metal/metal oxide catalyst, 40 mmol; water filling, 50%; 300 °C, 3 h.

Entry	Additives	$HCOO^-$ (mmol)	Hydrocarbons (mmol)			
			CH_4	C_2H_6	C_3H_8	C_6H_{14}~$C_{21}H_{44}$
1	Co	19.38	7.81	0.94	0.74	0.71
2	Co*	10.91	1.78	0.14	0.15	−
3	Ni	6.58	17.51	1.20	0.25	−
4	Cu	46.18	0.62	−	−	−
5	Mo	36.04	−	−	−	−
6	TiO_2	15.68	−	−	−	−
7	ZnO	27.86	−	−	−	−
8	Al_2O_3	18.26	−	−	−	−
9	−	42.23	0.47	−	−	−

* Experimental conditions: Fe, 40 mmol; $NaHCO_3$, 40 mmol; Co, 40 mmol; water filling, 50%; 300 °C, 3 h.

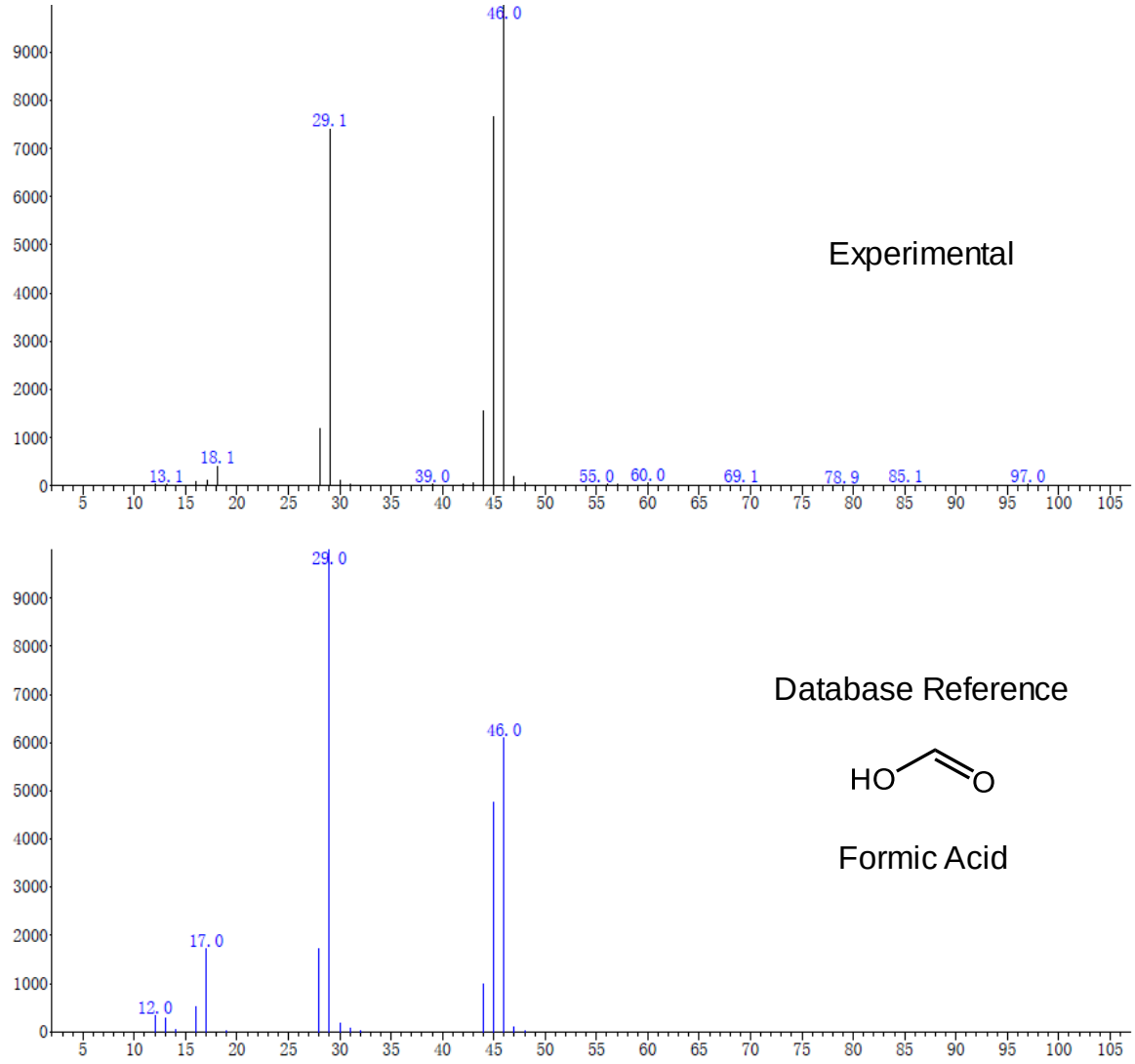

Fig. S1. GC-MS analysis. Mass spectrometry data for formic acid.

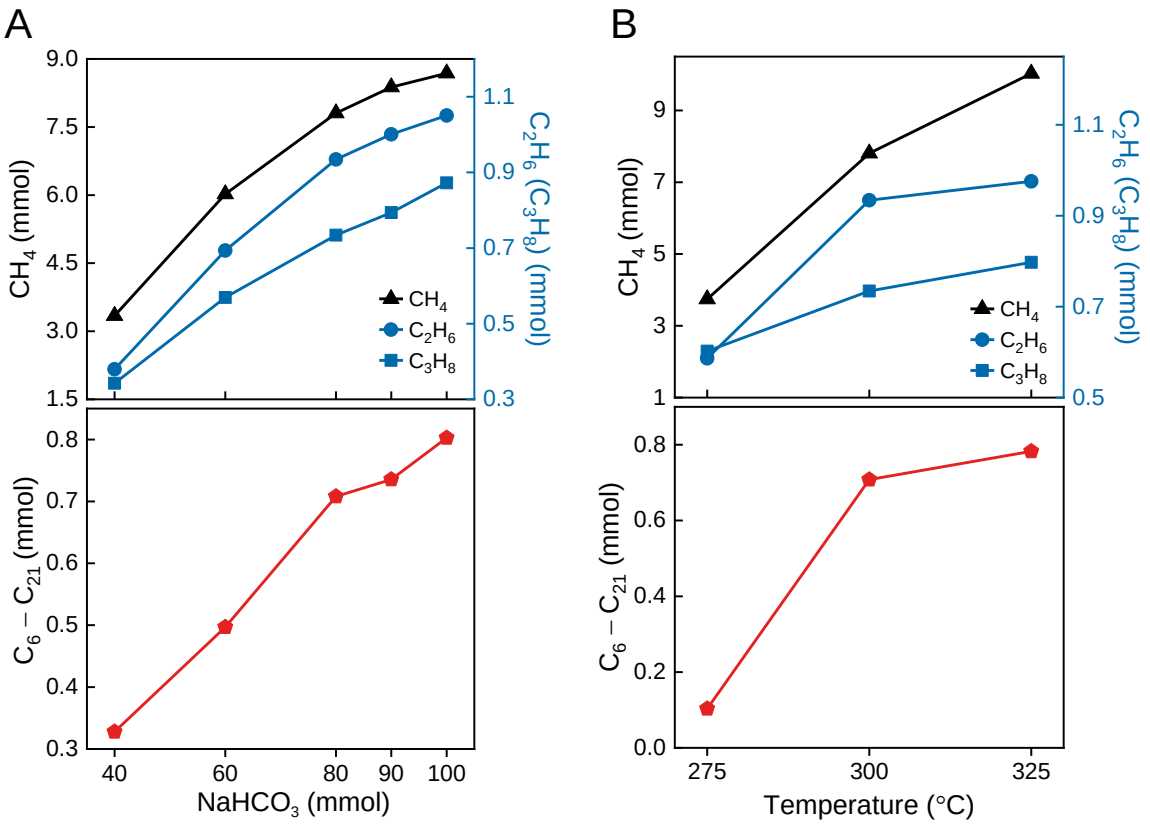

Fig. S2. Kinetic experiments of concentration and temperature. (A) Kinetic curves of hydrothermal production of C_1~C_3 (upper panel) and C_6~C_{21} (bottom panel) alkanes with different amount of $NaHCO_3$. Experimental conditions: Fe, 80 mmol; Co, 40 mmol; water filling, 50%; 300 °C, 3 h. (B) Temperature-dependent production of C_1~C_3 (upper panel) and C_6~C_{21} (bottom panel) from $NaHCO_3$ reduction. Experimental conditions: Fe, 80 mmol; $NaHCO_3$, 80 mmol; Co, 40 mmol; water filling, 50%; 3 h.

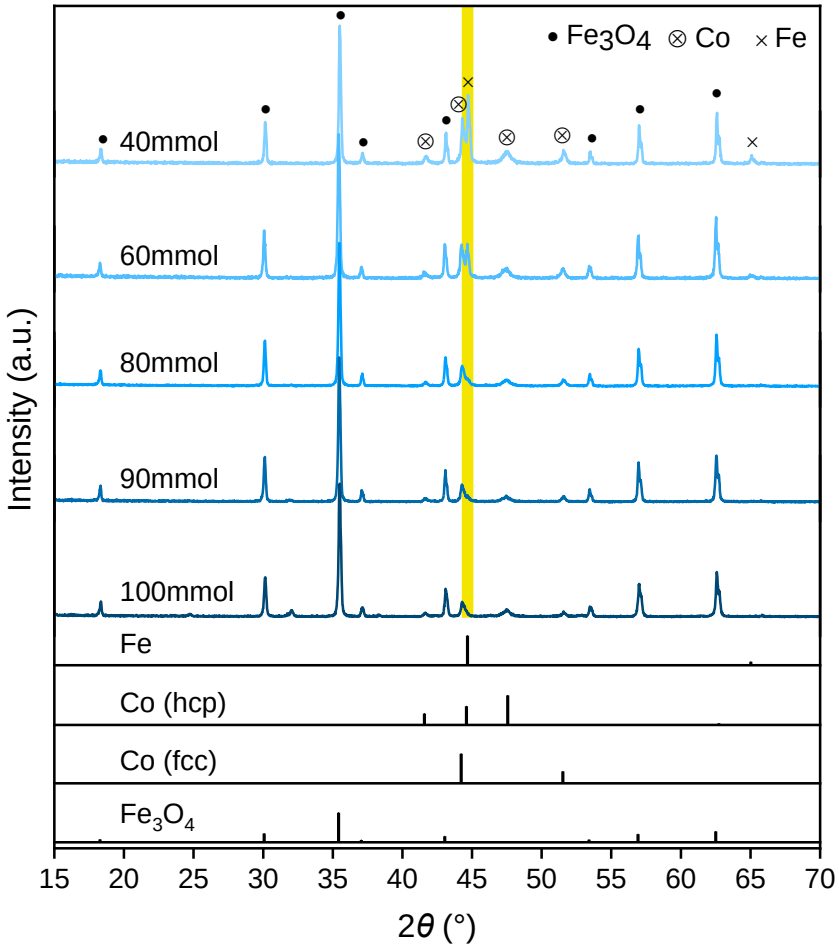

Fig. S3. XRD analysis. XRD patterns of the solid sample after hydrothermal reaction with different amount of $NaHCO_3$. Experimental conditions: Fe, 80 mmol; Co, 40 mmol; water filling, 50%; 300 °C, 3 h. The vertical black lines are the XRD peaks of standard Fe (JCPDS No. 89-7194), Co (JCPDS No. 01-1278 for hcp and No. 15-0806 for fcc), and Fe_3O_4 (JCPDS No. 79-0418).

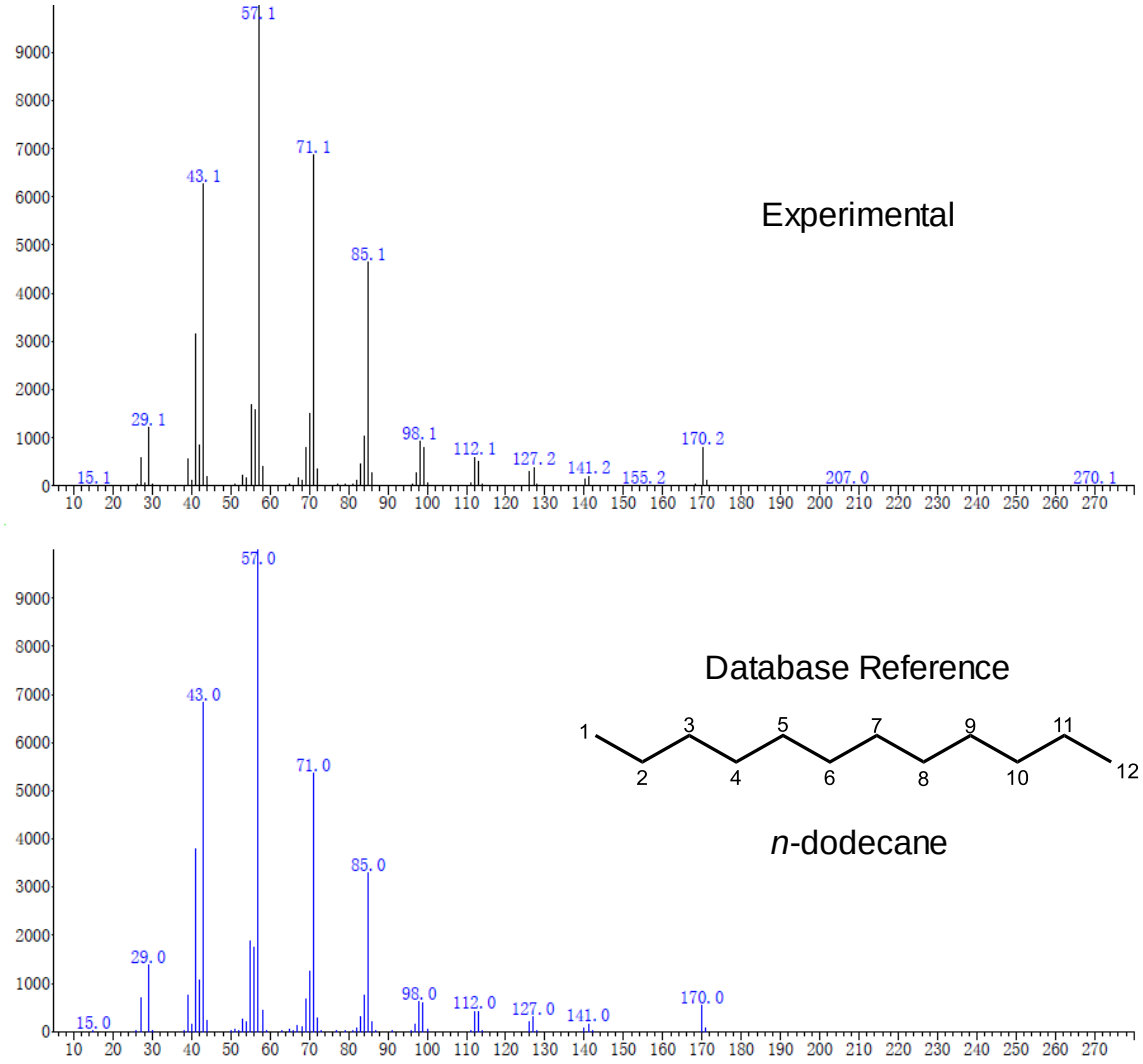

Fig. S4. GC-MS analysis. Mass spectrometry data for *n*-dodecane.

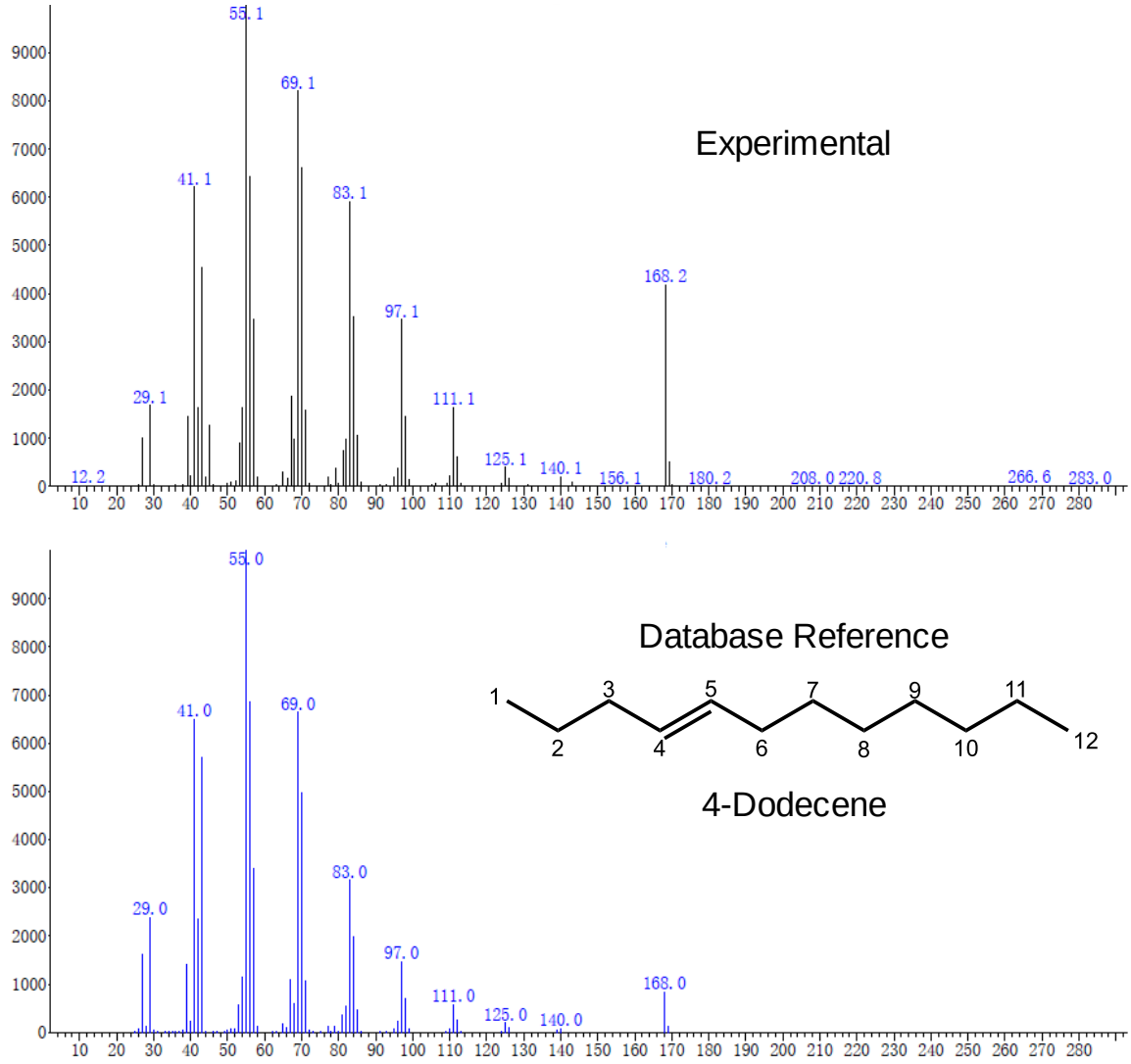

Fig. S5. GC-MS analysis. Mass spectrometry data for 4-Dodecene.

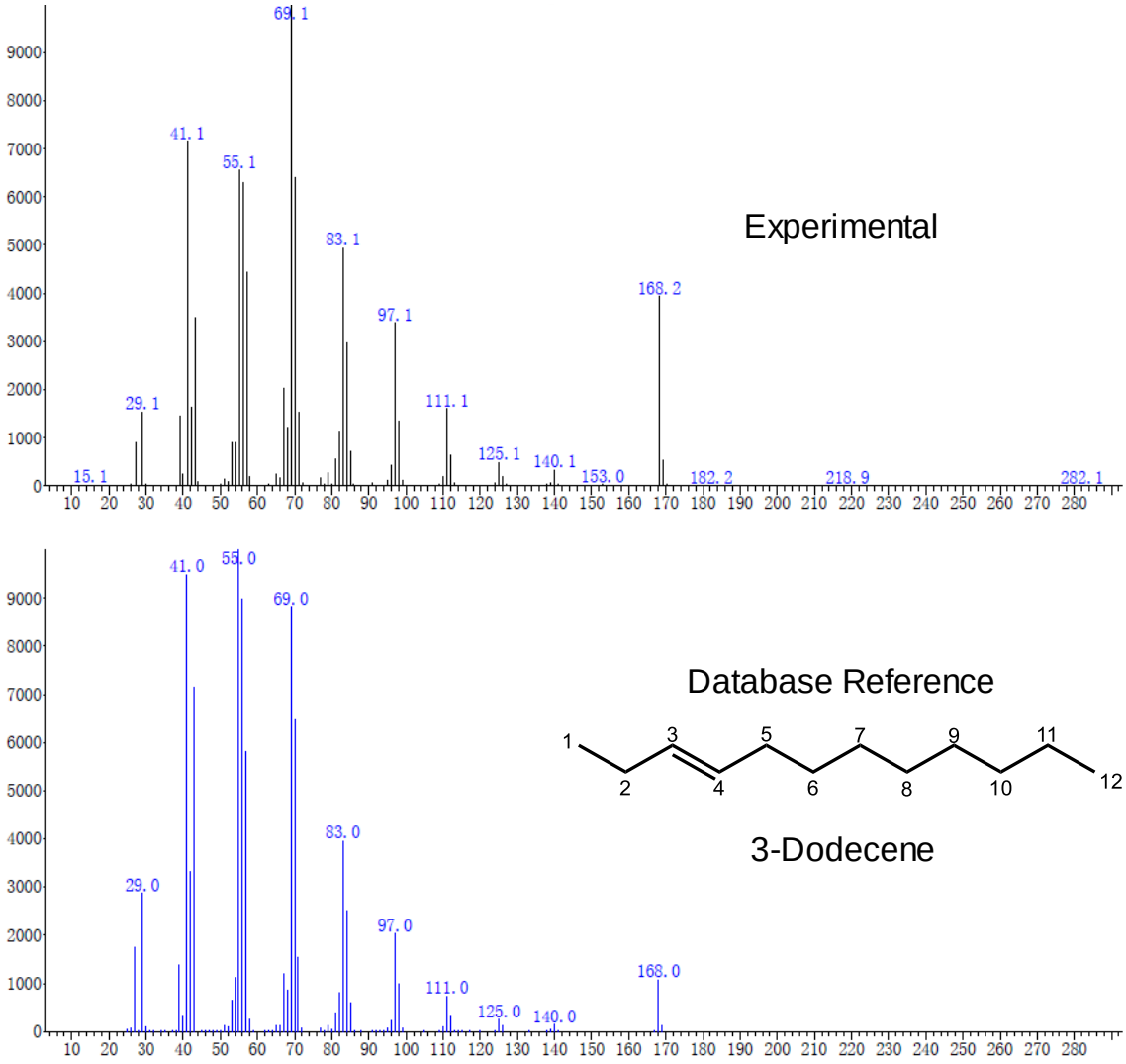

Fig. S6. GC-MS analysis. Mass spectrometry data for 3-Dodecene.

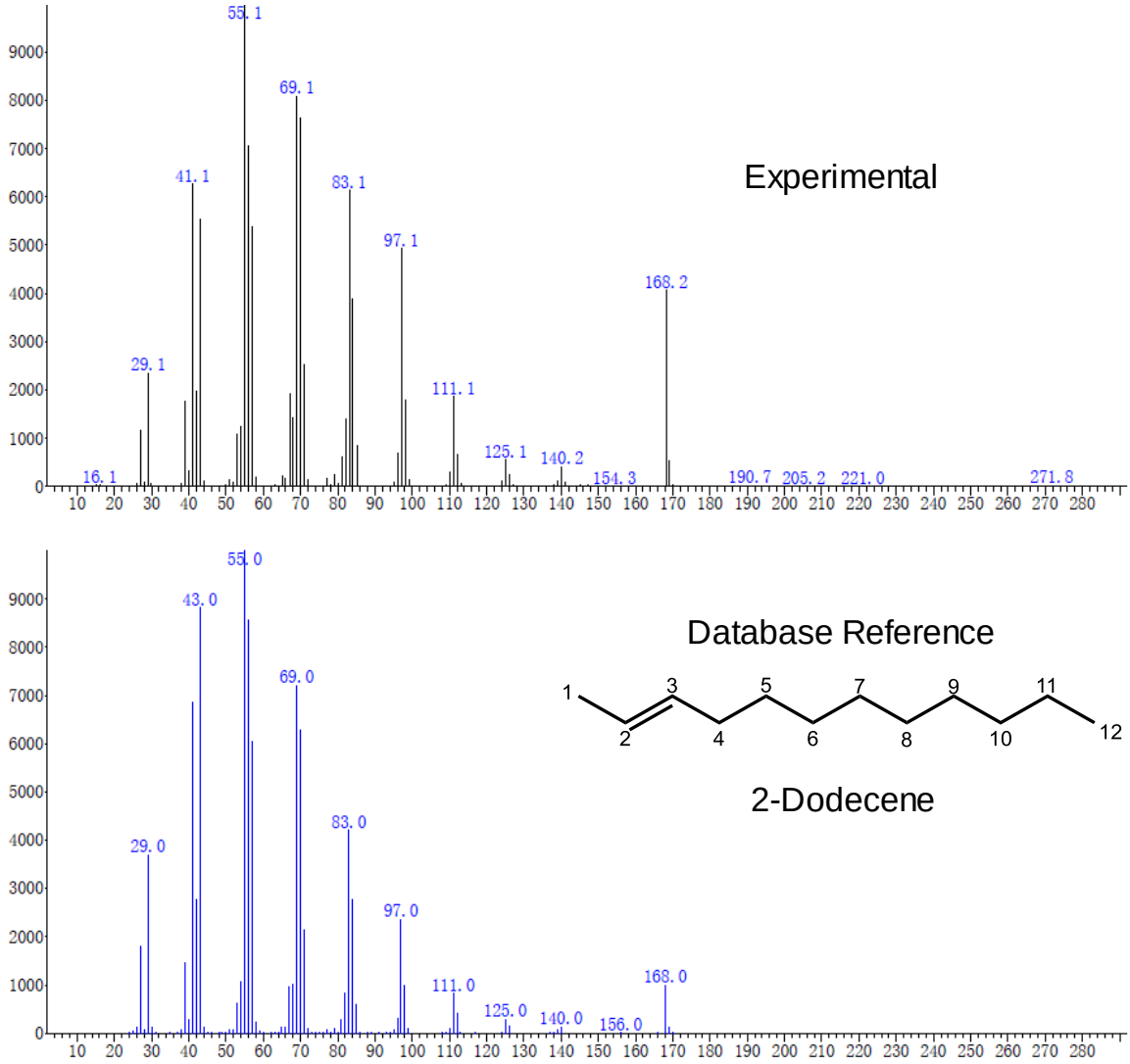

Fig. S7. GC-MS analysis. Mass spectrometry data for 2-Dodecene.

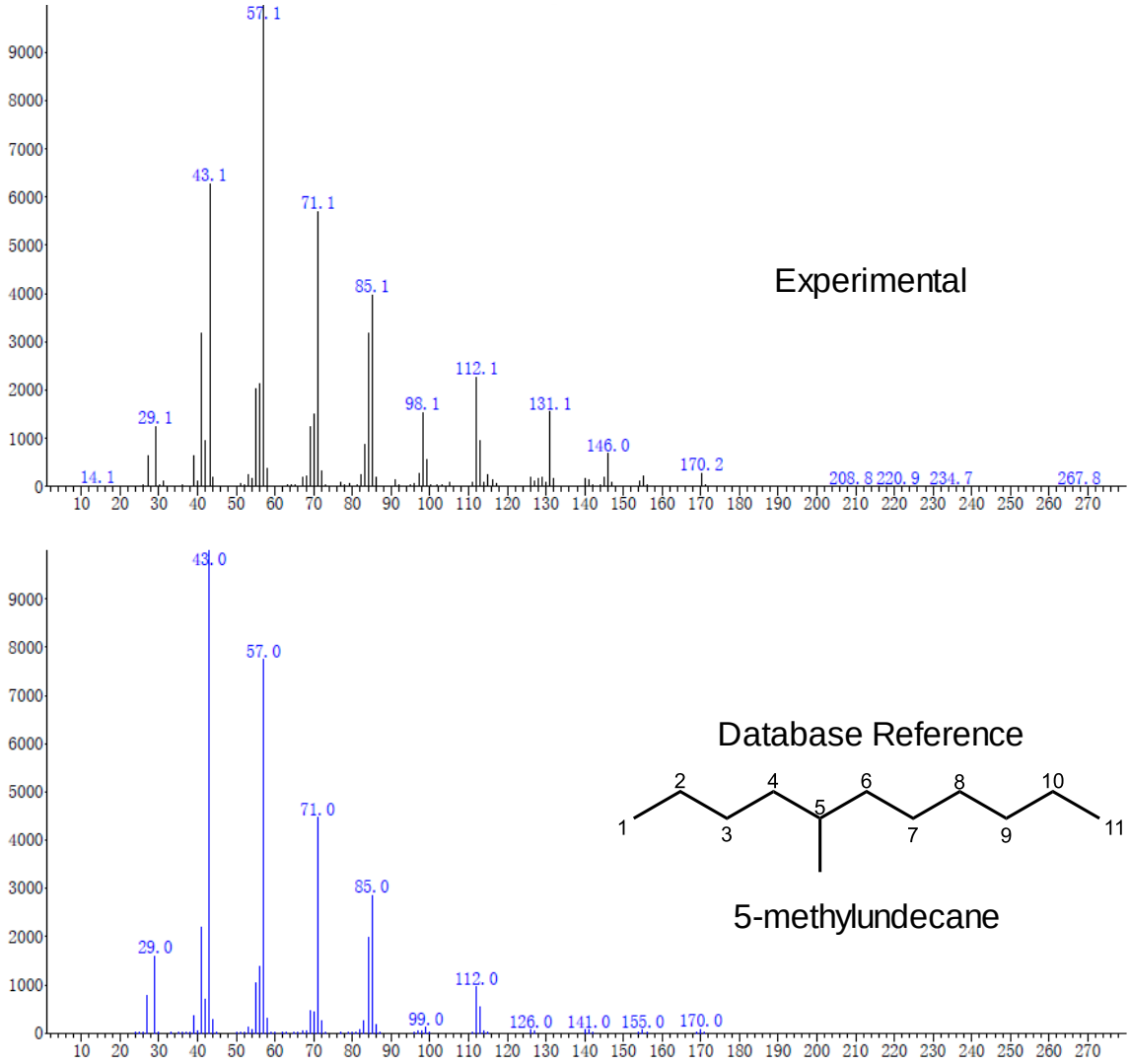

Fig. S8. GC-MS analysis. Mass spectrometry data for 5-methylundecane.

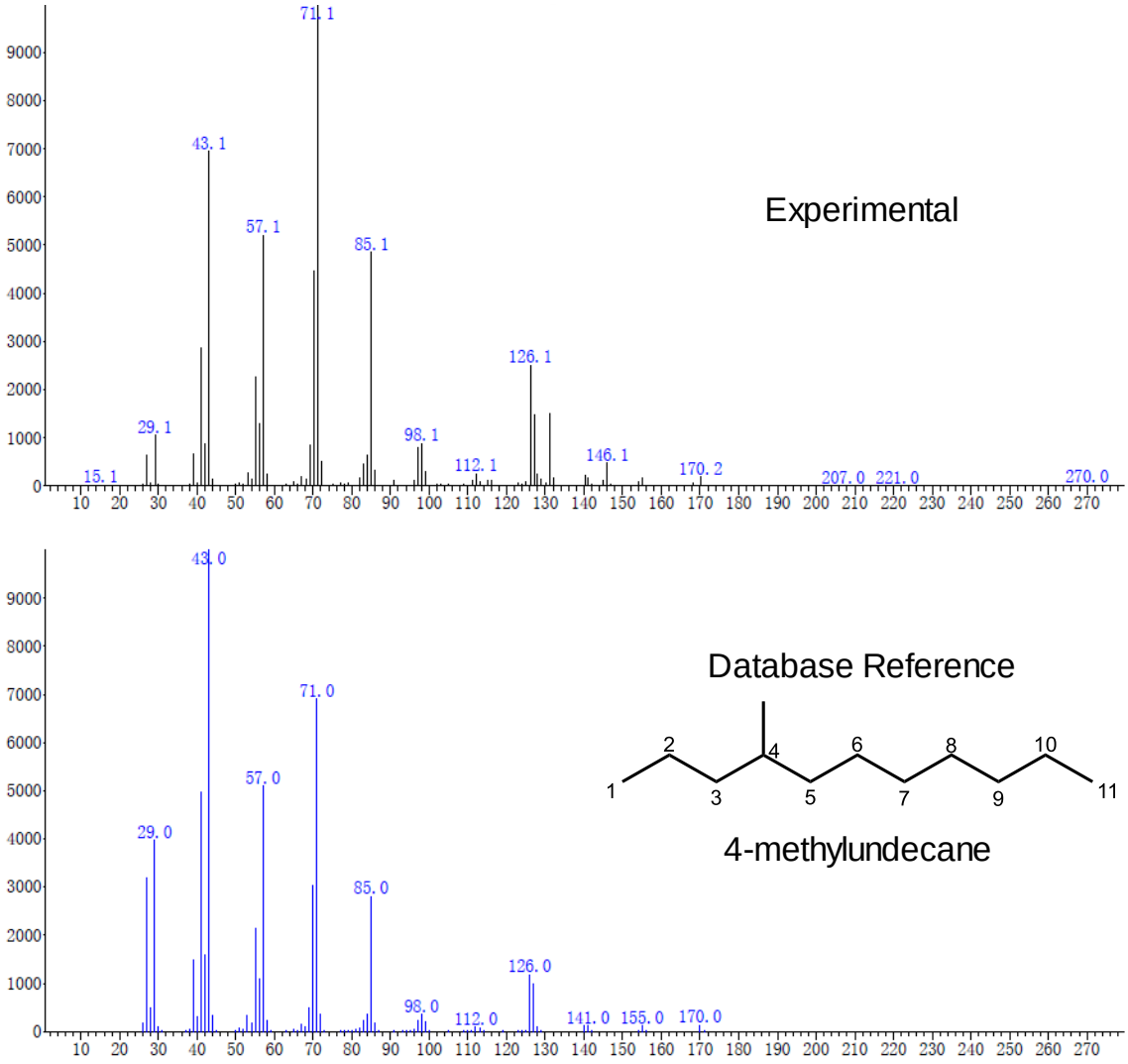

Fig. S9. GC-MS analysis. Mass spectrometry data for 4-methylundecane.

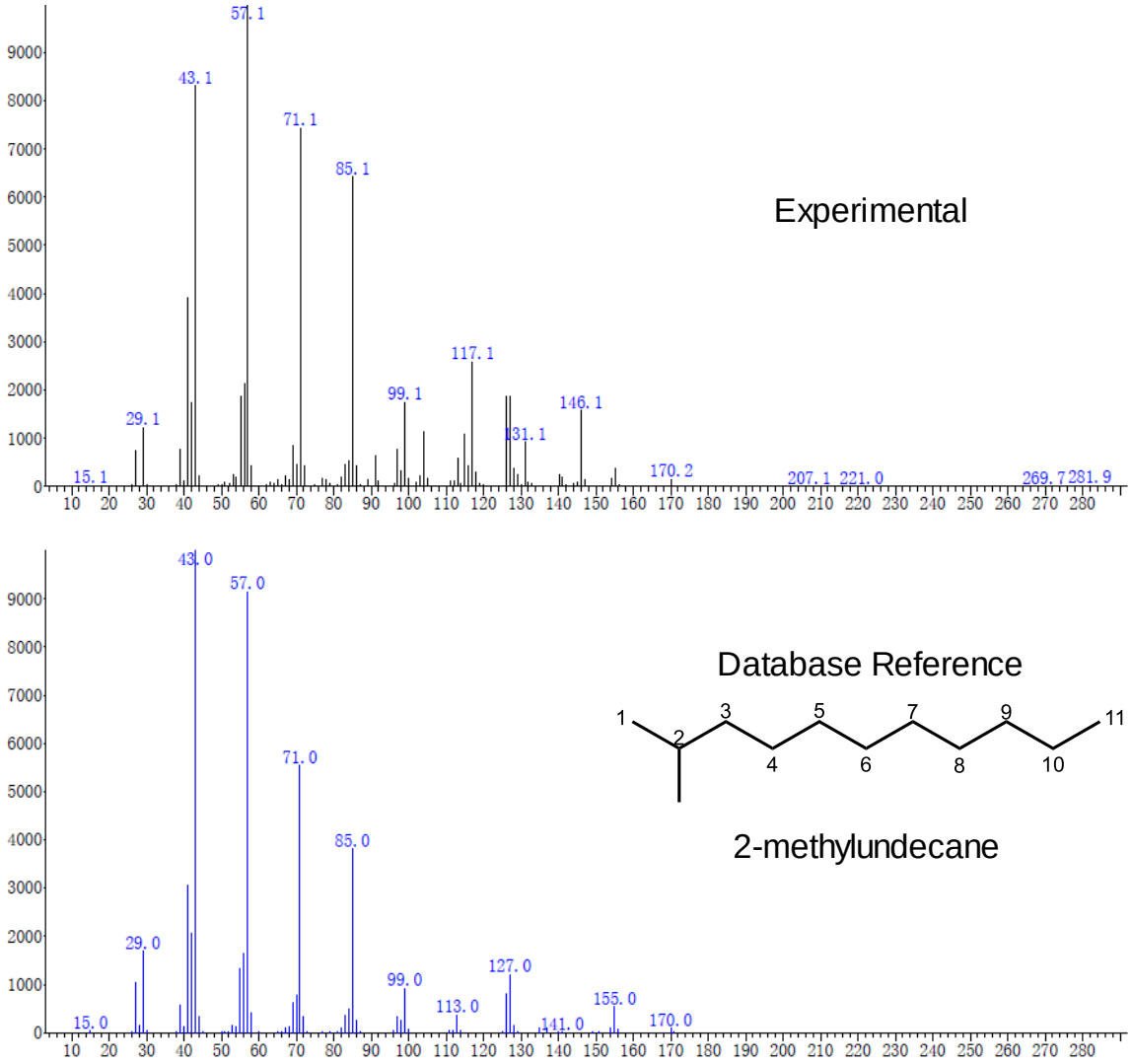

Fig. S10. GC-MS analysis. Mass spectrometry data for 2-methylundecane.

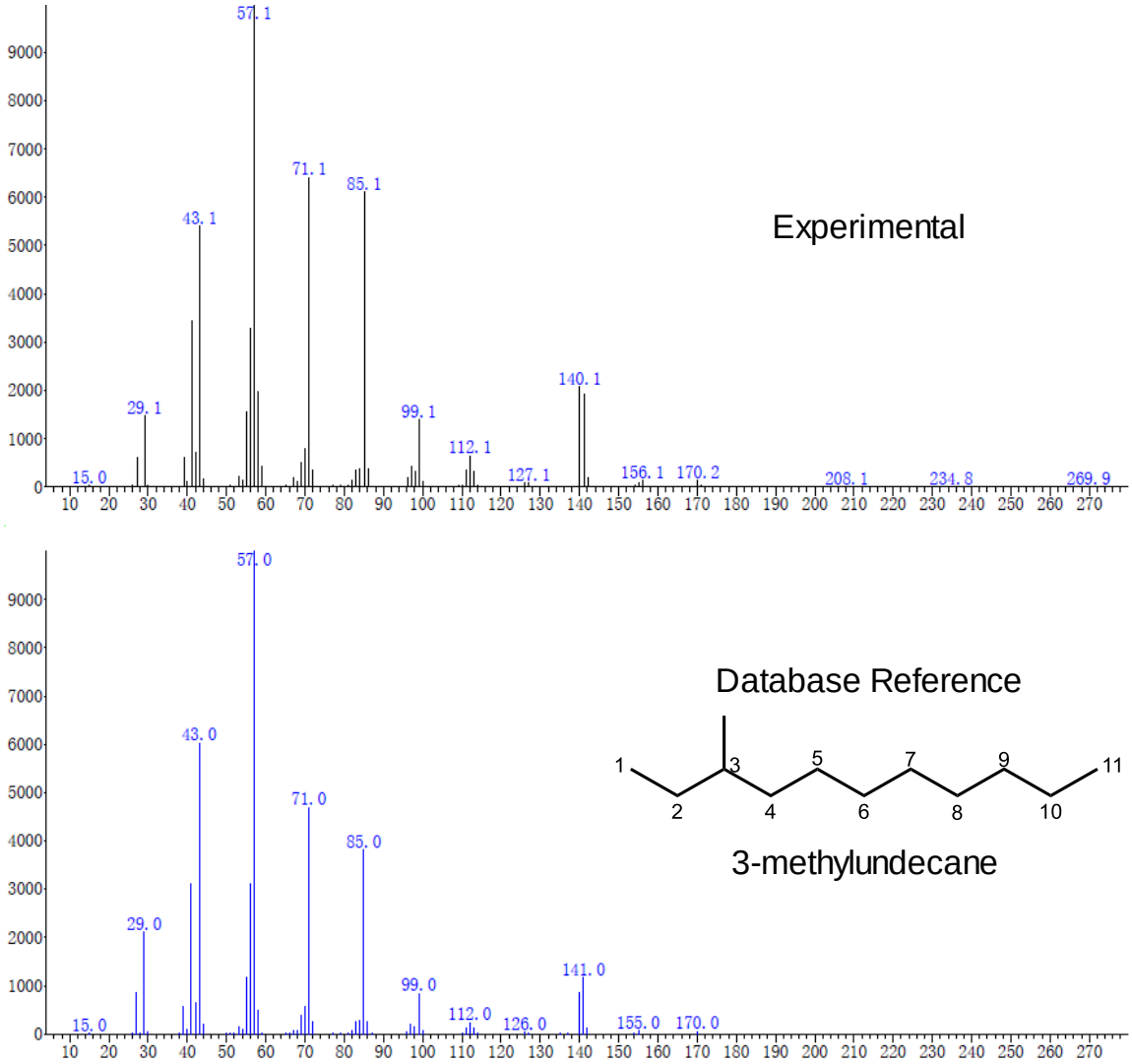

Fig. S11. GC-MS analysis. Mass spectrometry data for 3-methylundecane.

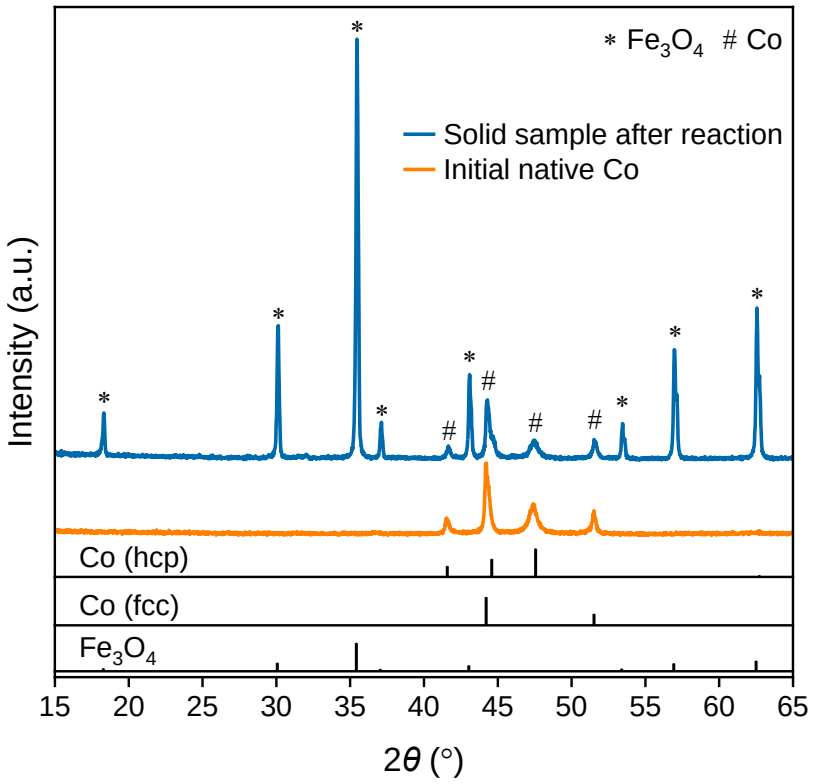

Fig. S12. XRD analysis. XRD patterns of the solid sample after hydrothermal reaction (blue line) . The Fe was oxidized into magnetite (Fe_3O_4) while Co maintained its initial native valence state (orange line). Experimental conditions: Fe, 80 mmol; $NaHCO_3$, 80 mmol; Co, 40 mmol; water filling, 50%; 300 °C, 3 h. The vertical black lines are the XRD peaks of standard Co (JCPDS No. 01-1278 for hcp and No. 15-0806 for fcc) and Fe_3O_4 (JCPDS No. 79-0418).

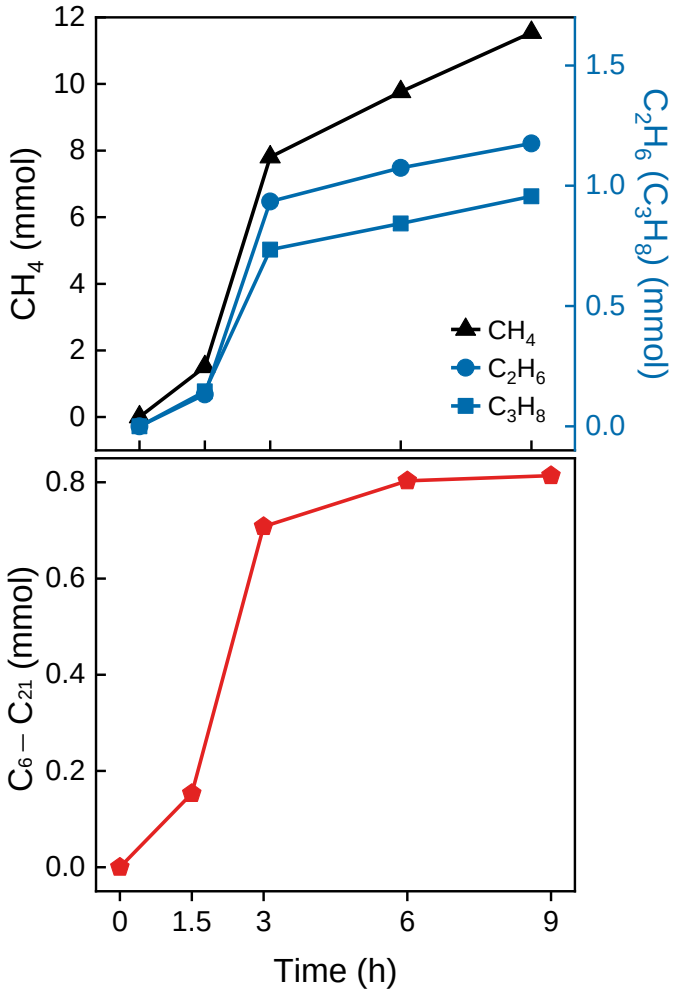

Fig. S13. Time course of hydrothermal reaction. Kinetic curves of hydrothermal production of C_1~C_3 (upper panel) and C_6~C_{21} (bottom panel) alkanes as a function of reaction time. Experimental conditions: Fe, 80 mmol; $NaHCO_3$, 80 mmol; Co, 40 mmol; water filling, 50%; 300 °C.

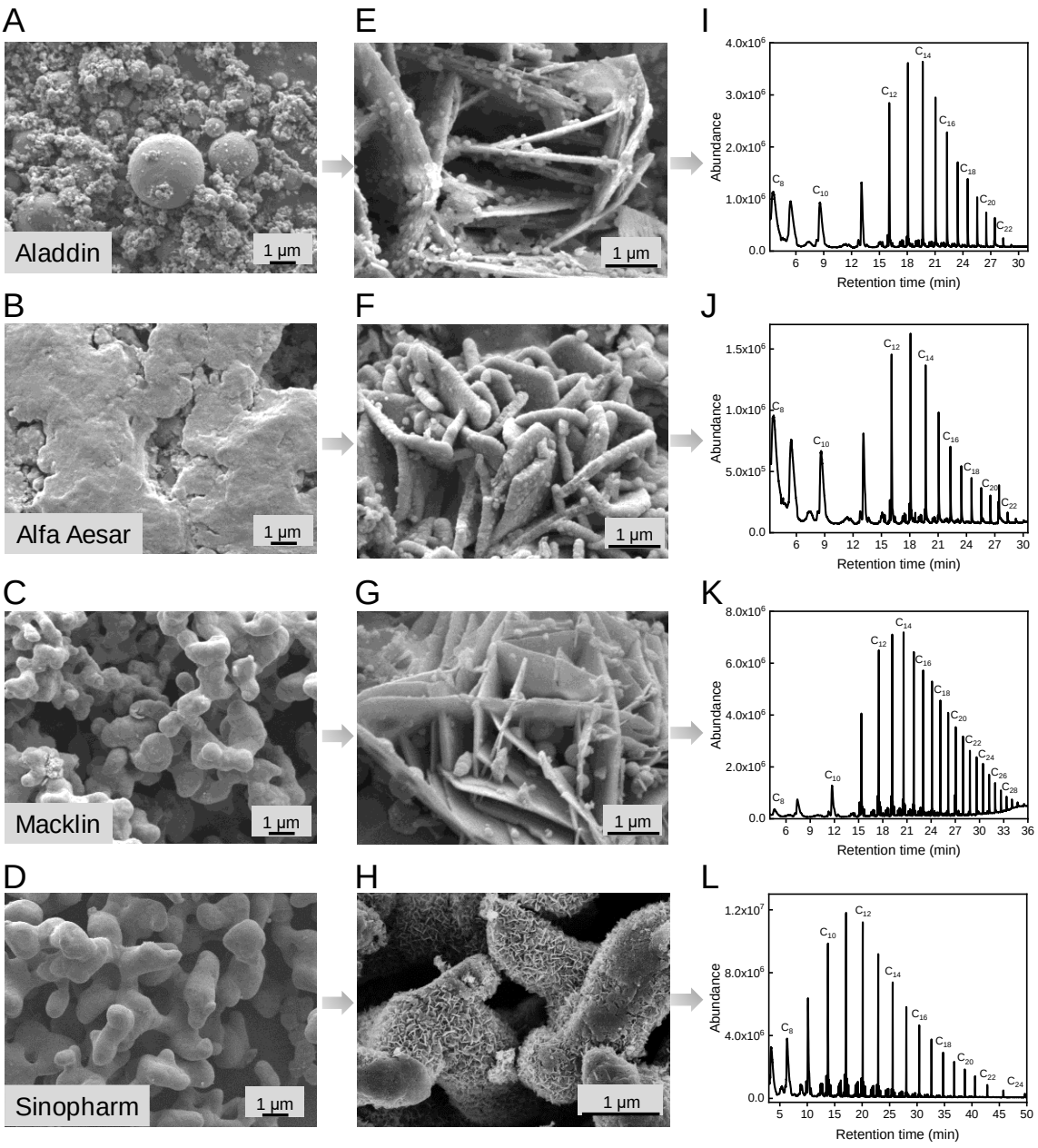

Fig. S14. Morphology evolution of Co. SEM images of Co samples obtained from different companies before reaction (A−D), after hydrothermal reaction (E−H), and the total ion chromatogram (I−L) from GC-MS analysis of its catalytic hydrocarbons production. The commercial Co powder was purchased from Aladdin (A), Alfa Aesar (B), and Macklin (C), and Sinopharm (D) Company, respectively. Experimental conditions: Fe, 80 mmol; $NaHCO_3$, 80 mmol; Co, 40 mmol; water filling, 50%; 300 °C, 3 h.

According to the proposed mechanism of the origin of honeycomb Co nanosheets, the formation of honeycomb Co nanosheets should not be limited to the initial morphology of Co. To test this hypothesis, we investigated the formation of long-chain hydrocarbons and honeycomb Co

nanosheets with different commercial Co powders in the reduction of $NaHCO_3$. It was demonstrated that powder Co obtained from different companies could catalyze the formation of hydrocarbons and honeycomb-like nanosheets under the same conditions, further supporting the mechanism of Co stability by the dissolution and reprecipitation process and indicating that the formation of long-chain hydrocarbons is not dependent on the initial Co morphology, which is significant for industrial and environmental applications.

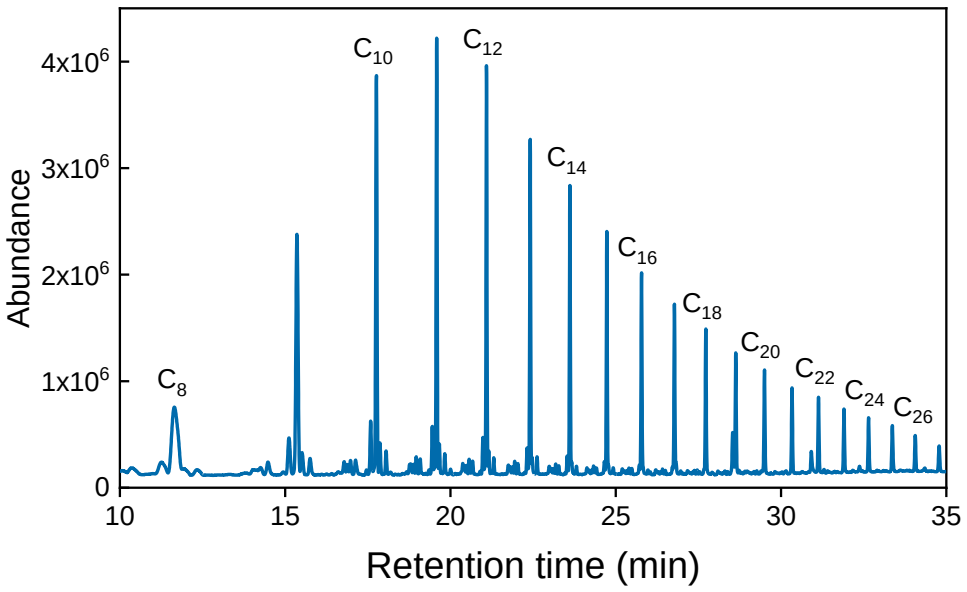

Fig. S15. Performance of recycled catalyst. GC-MS analysis of hydrothermal $NaHCO_3$ reduction with H_2 gas using the recycled Co−Fe_3O_4 catalyst. We tested the catalytic activity of the recycled Co−Fe_3O_4 catalyst with an external H_2 reductant. Experimental conditions: H_2, 5 MPa; $NaHCO_3$, 80 mmol; water filling, 50%; 300 °C, 3 h. The formation of long-chain hydrocarbons was clearly observed, indicating the high catalytic activity of the formed Co−Fe_3O_4 catalyst for synthesizing long-chain hydrocarbons. This result suggests the fundamental role of honeycomb Co nanosheets in prebiotic organic synthesis and introduces a new approach for synthesizing long-chain hydrocarbons by nonnoble metal catalysts in conventional CO_2 hydrogenation.

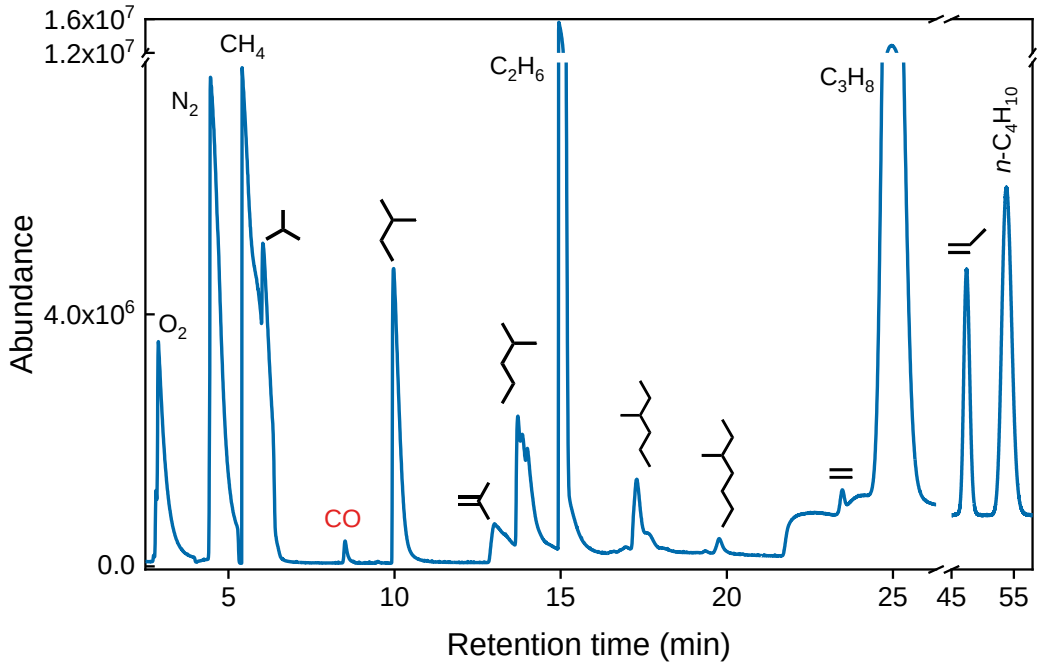

Fig. S16. GC-MS analysis. Total ion chromatogram from GC-MS analysis of the gas products. The GC-MS analysis showed that CO was formed. Experimental conditions: Fe, 80 mmol; $NaHCO_3$, 80 mmol; Co, 40 mmol; water filling, 50%; 300 °C, 3 h.

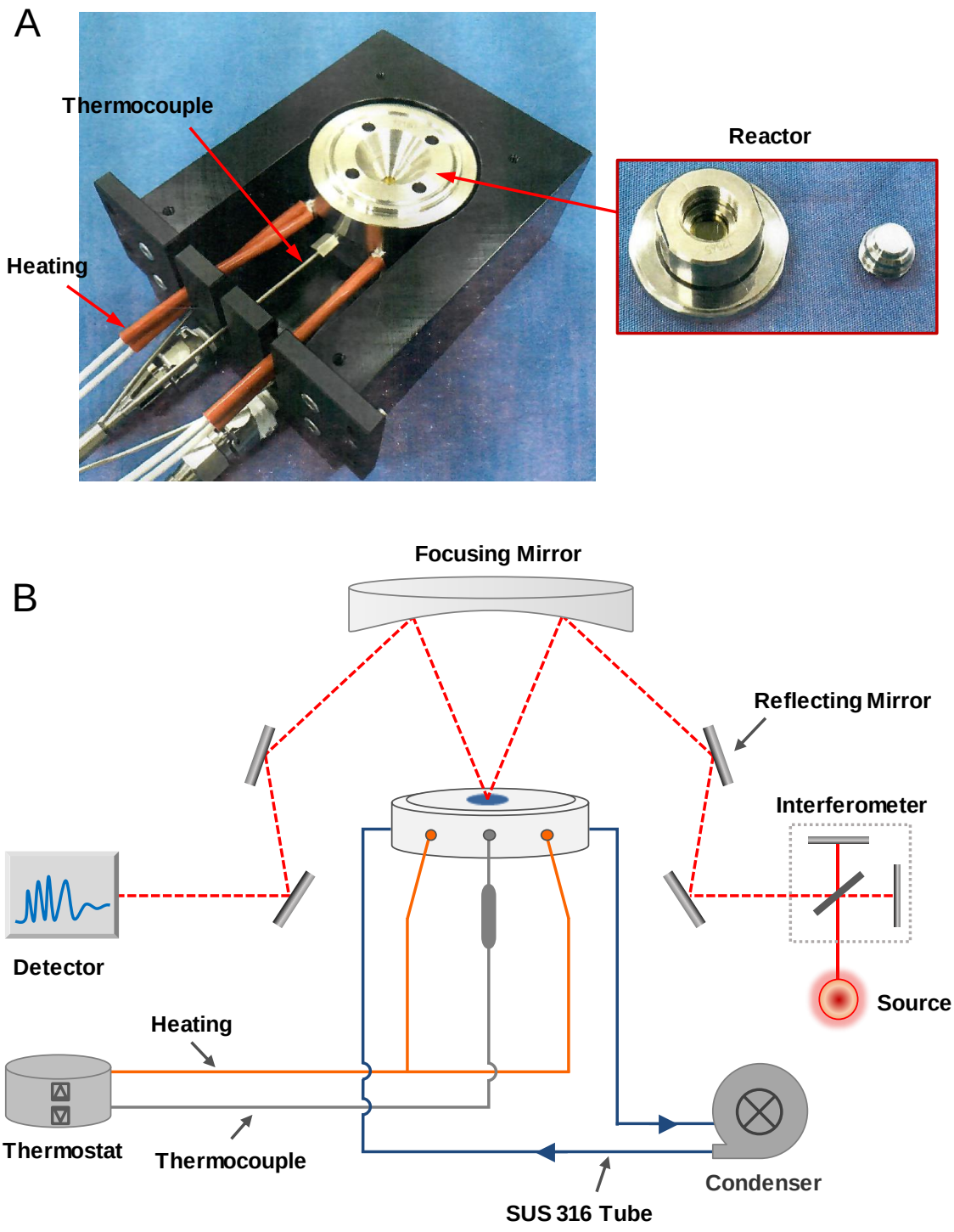

Fig. S17. Schematic of operando high-pressure and high-temperature ATR-FTIR cell. (A) Photo of high-pressure and high-temperature reactor. (B) Schematic of the whole operando ATR-FTIR system.

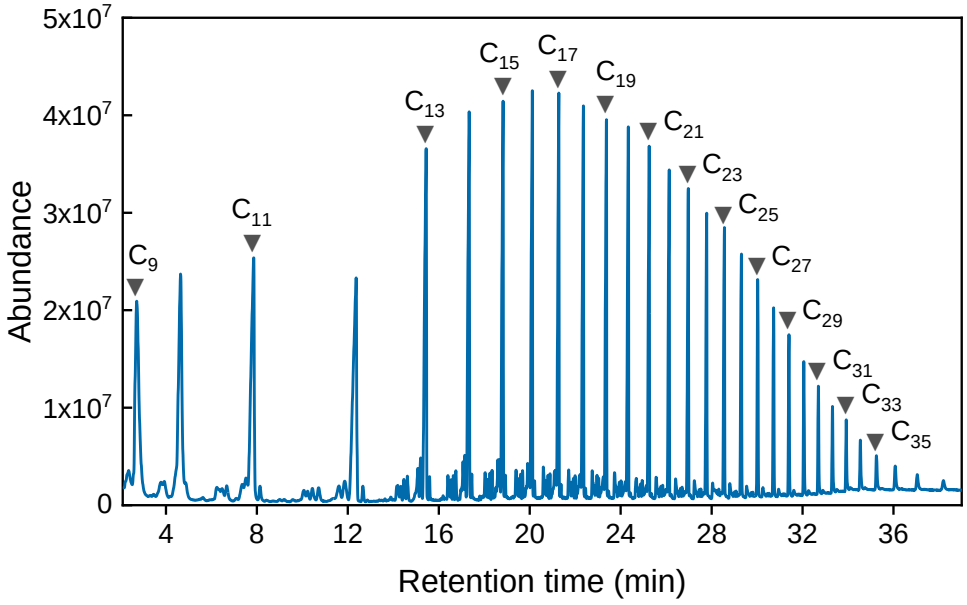

Fig. S18. GC-MS analysis. Total ion chromatogram from GC-MS analysis of hydrothermal CO reduction. The experiment with CO as the initial carbon source for substituting $NaHCO_3$ under the same conditions also generated long-chain hydrocarbons. Experimental conditions: Fe, 80 mmol; CO, 5 MPa; Co, 40 mmol; water filling, 50%; 300 °C, 3 h, pH 8.

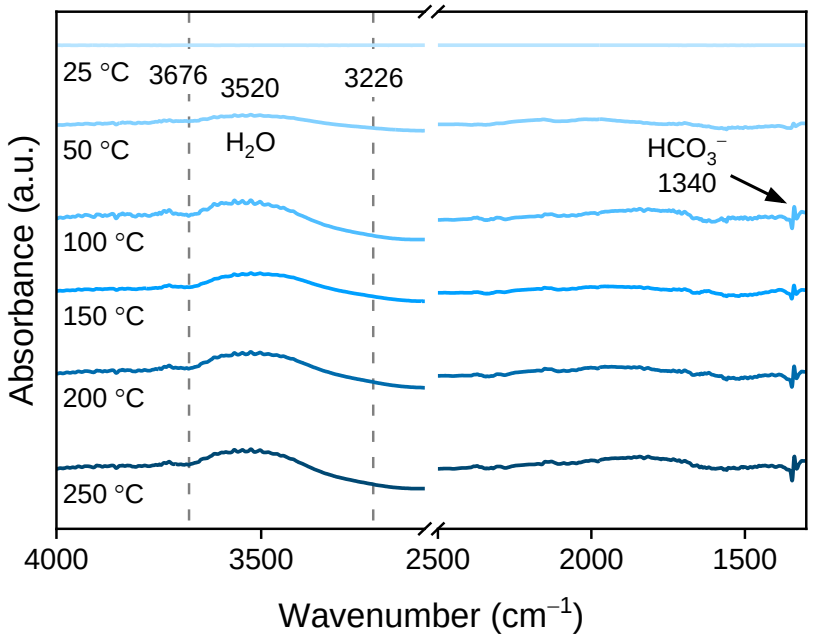

Fig. S19. ATR-FTIR spectra. Operando ATR-FTIR spectra of $NaHCO_3$ reduction by Fe in the absence of Co. The peak from the hydroxyl group in Fe−OH located at 3676 and 3226 cm^{-1} disappeared in the absence of Co.

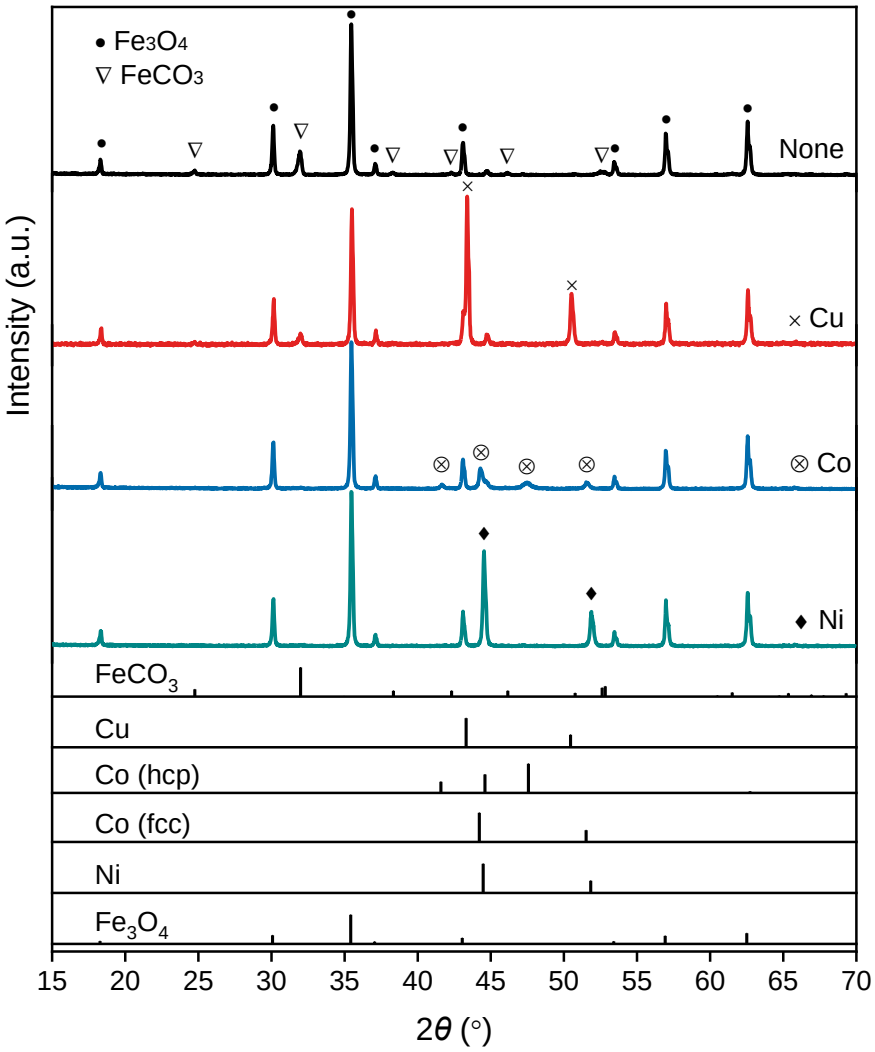

Fig. S20. XRD analysis. XRD patterns of the solid samples after hydrothermal reactions with different transition metals. The formation of $FeCO_3$ was inhibited by increasing the adsorption energy of COOH on the metal surface. Experimental conditions: Fe, 80 mmol; $NaHCO_3$, 80 mmol; Cu/Co/Ni, 40 mmol; water filling, 50%; 300 °C, 3 h. The vertical black lines are the XRD peaks of standard $FeCO_3$ (JCPDS No. 29-0696), Cu (JCPDS No. 85-1326), Co (JCPDS No. 01-1278 for hcp and No. 15-0806 for fcc), Ni (JCPDS No. 70-1849), and Fe_3O_4 (JCPDS No. 79-0418).

SI References

1. Martin, W., Baross, J., Kelley, D. & Russell, M.J. Hydrothermal vents and the origin of life. *Nat. Rev. Microbiol.* **6**, 805-814 (2008).
2. Horita, J. & Berndt, M.E. Abiogenic methane formation and isotopic fractionation under hydrothermal conditions. *Science* **285**, 1055-1057 (1999).
3. Sverjensky, D.A., Stagno, V. & Huang, F. Important role for organic carbon in subduction-zone fluids in the deep carbon cycle. *Nat. Geosci.* **7**, 909-913 (2014).
4. McCollom, T.M., Lollar, B.S., Lacrampe-Couloume, G. & Seewald, J.S. The influence of carbon source on abiotic organic synthesis and carbon isotope fractionation under hydrothermal conditions. *Geochim. Cosmochim. Acta* **74**, 2717-2740 (2010).
5. McCollom, T.M. Abiotic methane formation during experimental serpentinization of olivine. *Proc. Natl. Acad. Sci. U.S.A.* **113**, 13965-13970 (2016).
6. McCollom, T.M. Laboratory Simulations of Abiotic Hydrocarbon Formation in Earth's Deep Subsurface. *Rev. Mineral. Geochem.* **75**, 467-494 (2013).
7. Ueda, H. & Shibuya, T. Composition of the Primordial Ocean Just after Its Formation: Constraints from the Reactions between the Primitive Crust and a Strongly Acidic, CO_2-Rich Fluid at Elevated Temperatures and Pressures. *Minerals* **11**, 389 (2021).